

# Reconstruction Performance Studies with MicroBooNE Data in Support of Summer 2018 Analyses

MICROBOONE-NOTE-1049-PUB

MicroBooNE Collaboration

June 1, 2018

## **Abstract**

In this note we present a number of reconstruction performance measurements conducted on MicroBooNE data. Results show good agreement between the data and the predictions from simulation, thus validating the version of the reconstruction used by MicroBooNE analyses, which are presented at 2018 conferences. The observed level of performance shows the high level of resolution obtainable with a large-scale LArTPC imaging detector. Tracking and vertexing resolutions at or below the millimeter scale are obtained for neutrino interaction event reconstruction. Energy reconstruction measurements are presented for tracks and EM showers using multiple Coulomb scattering and calorimetry respectively; in the case of EM showers these represent the first result obtained in a fully-automated reconstruction chain. Nevertheless, the present results are expected to improve with further refinements of the employed reconstruction algorithms. The techniques which are presented here have a broader validity than MicroBooNE and could be applied to other LArTPC detectors as they start taking data in the next months or years.

# Contents

<b>1</b>	<b>Introduction</b>	<b>3</b>
<b>2</b>	<b>Overview of Reconstruction in MicroBooNE</b>	<b>3</b>
2.1	Higher-level Reconstruction Algorithms . . . . .	6
2.1.1	Momentum measurement from Multiple Coulomb Scattering . . . . .	6
2.1.2	Kalman filter fit of tracks . . . . .	6
2.1.3	Geometric fit of 3D vertex position . . . . .	7
2.1.4	Shower reconstruction for photons from $\pi^0$ decays . . . . .	8
2.2	Samples and Event Selection . . . . .	9
<b>3</b>	<b>Data-driven Performance Studies</b>	<b>10</b>
3.1	Momentum Measurement for Exiting Tracks . . . . .	10
3.2	Track Position and Direction Resolution . . . . .	14
3.3	Vertex Resolution . . . . .	19
3.4	Shower Energy Corrections and $\pi^0$ Mass Peak Reconstruction . . . . .	23
<b>4</b>	<b>Conclusions</b>	<b>28</b>

# 1 Introduction

The MicroBooNE [1] experiment at Fermilab consists of a Liquid Argon Time Projection Chamber (LArTPC) exposed to neutrinos from the Booster Neutrino Beam (BNB) and from an off-axis component of the NuMI beam. MicroBooNE is the latest among a family of detectors that exploit the potential of liquid argon as the detection medium for neutrino interactions. Next generation LArTPCs for the Short Baseline Neutrino (SBN) program [2] and the Deep Underground Neutrino Experiment (DUNE) [3] are now being designed and constructed. The main physics goals of MicroBooNE are to address short baseline neutrino oscillations, primarily the MiniBooNE observation of an excess of electron-like events at low energy [4], as well as to perform high precision measurements of neutrino-argon cross sections.

Studies of reconstruction performance in data are important for experiments to gauge detector systematic uncertainties, to validate signal processing and reconstruction developments, and to demonstrate the achieved performance with the detector technology of the experiment. Developing techniques for data-driven studies is particularly important at the present time, with several new LArTPC detectors not far from their commissioning phase; in fact, applying similar techniques to multiple experiments will allow a direct comparison of their performance and a better understanding of systematic effects across experiments. MicroBooNE has previously published data-driven results related to reconstruction efficiencies of cosmic ray tracks [5], the reconstruction of Michel electrons [6], and the measurement of momentum for contained muon tracks [7].

This note is a collection of data-driven reconstruction performance studies in support of analyses presented for the first time at the Neutrino 2018 conference. As such, results are intended to demonstrate the level of understanding of the MicroBooNE reconstruction performance in data as per the 2018 production campaign. While the techniques presented here can be used to evaluate the detector performance, the current versions of the algorithms have known limitations. The measured performance in this note therefore should not be construed as the final statement on MicroBooNE capabilities or on the LArTPC technology. Indeed, limitations and plans for improvements are discussed in this note.

## 2 Overview of Reconstruction in MicroBooNE

The MicroBooNE detector is a LArTPC (see Fig. 1 for a representation of the working principle of the detector) with dimensions of 256 cm (width)  $\times$  233 cm (height)  $\times$  1037 cm (length). The cryostat contains a total of 170 t of liquid argon, of which about 85 t are within the TPC boundaries. The  $x$  direction corresponds to the drift coordinate, the  $y$  direction is the vertical direction, and the  $z$  direction points along the beam (Fig. 2). Spherical coordinates are a representation particularly useful to describe directions:  $\theta = \tan^{-1}(r/z)$  is the angle with respect to the beam direction (where  $r = \sqrt{x^2 + y^2}$ ) and  $\phi = \tan^{-1}(y/x)$  is the azimuthal angle in the plane transverse to the beam. The TPC consists of three wire planes with 3 mm spacing at angles of 0, +60 and -60 degrees with respect to the vertical. The cathode operates at a voltage of -70 kV so that an electric field of 273 V/cm is produced.

In a neutrino interaction, a neutrino from the beam interacts with an argon nucleus, and the resulting charged particles traverse the liquid argon leaving an ionization trail which drifts to the anode planes with an average velocity of 0.11 cm/ $\mu$ s. Ionization electrons require a “drift time window” of 2.3 ms to travel the full 256 cm drift distance separating the anode and cathode. Charge drifting past a wire plane induces a current that produces a bipolar signal in the electronics. The

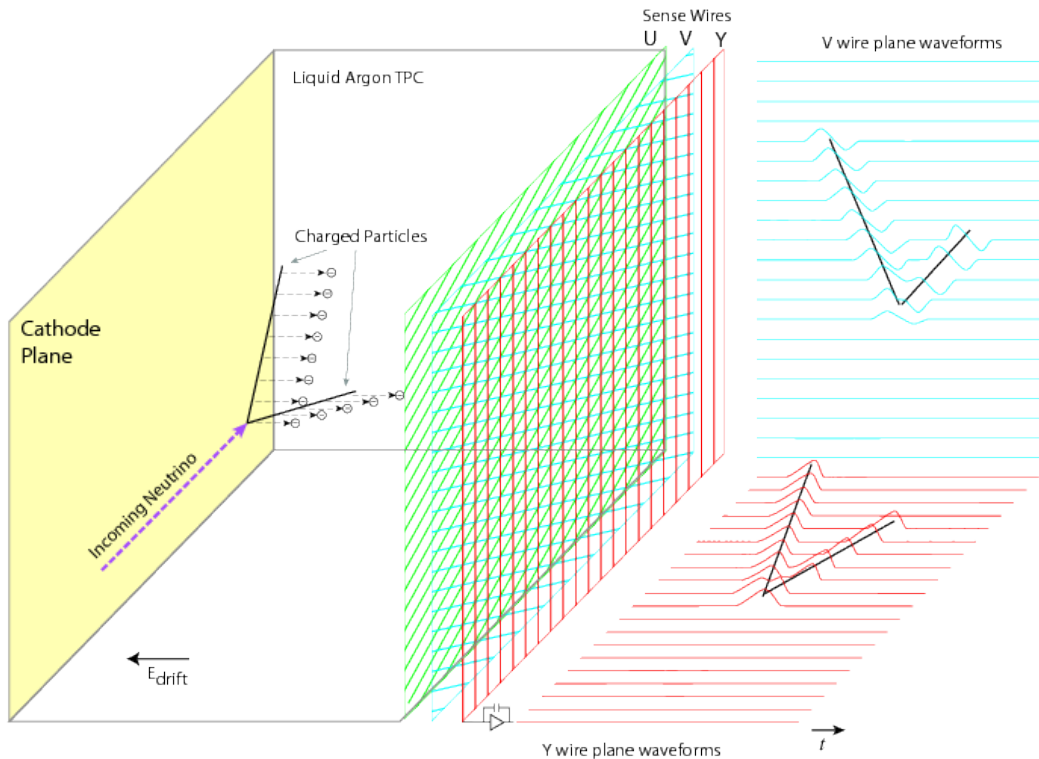


Figure 1: Operational principle of the MicroBooNE LArTPC.

first two planes are referred to as induction planes. The wire plane furthest from the cathode has wires oriented vertically; drifting electrons are collected on this plane producing a unipolar signal. The signals on each plane create distinct, two-dimensional projective views (in terms of wire and time) of the event, which can be combined to reconstruct a three-dimensional image of the interaction.

A set of 32 photomultiplier tubes (PMTs) is placed behind the anode plane to collect scintillation light from the argon. This light provides the start time for drifting electrons in an event with few-ns precision, and can be used for background suppression.

The detector is placed in a pit 6 m below the surface with no overburden, and is thus exposed to an abundant cosmic-ray muon flux. The rate in the MicroBooNE detector is estimated to be 5.5 kHz, which corresponds to about 13 muons per drift time window. More details about the MicroBooNE detector can be found in ref. [1].

The electric signal from the wires is digitized in a readout window of 4.8 ms (1.6 ms before plus 3.2 ms after the neutrino interaction time) with a clock frequency of 2 MHz by 12-bit analog to digital converters (ADCs). The digitized signals are first processed through noise filtering and deconvolution stages [8, 9, 10], where the deconvolution method applied to the data analyzed in this note is mono-dimensional (along time). The result of these signal processing stages are regions of interest (ROI) in the time domain characterized by unipolar waveform pulses with integrals proportional to the charge arriving at the readout wires. ROIs are further processed to reconstruct “hits”, containing the estimated position and amount of charge deposited on a wire

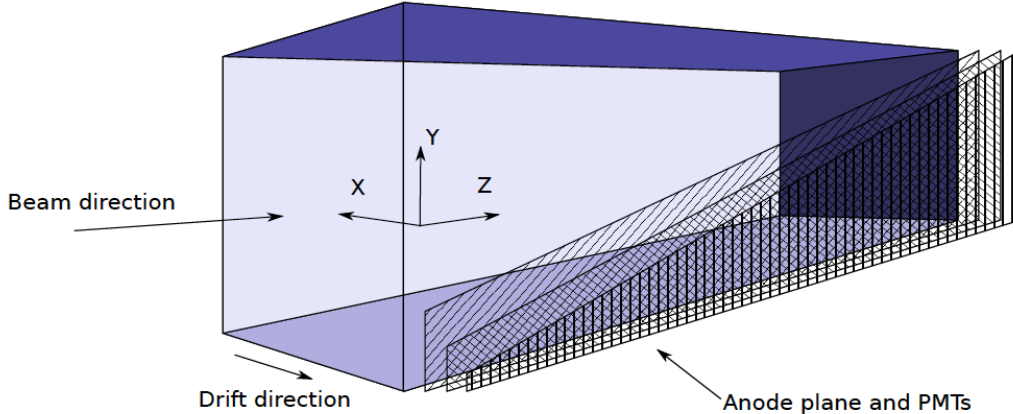


Figure 2: Definition of the global cartesian coordinate system.

by a single particle in the detector [11].

As a relatively new detector technology, higher level reconstruction in LArTPC experiments is currently a field undergoing active development, where a “standard” solution is still yet to be recognized in the community. Indeed, MicroBooNE is the first large-scale LArTPC experiment to feature a fully automated event reconstruction; this pioneering role has led to the exploration of multiple high-level reconstruction paradigms. Pandora [12] and TrajCluster [11] are a set of pattern recognition algorithms clustering hits in different planes and matching those clusters in three dimensions to identify the trajectory of each particle in the event. The WireCell [13] paradigm is an approach inspired by tomographic imaging which, by leveraging charge and sparsity information, aims to identify energy deposits in 3D prior to clustering trajectories directly in 3D. The last paradigm is based on deep learning techniques [14], and uses convolutional neural networks to identify features and different particle species in an event associated to neutrino interactions; features are extracted from 2D images obtained from each wire-plane, where the axes are defined by wire number and readout time, and the pixel content corresponds to the collected charge expressed in ADC counts. It is worth noting that the different paradigms employed in the MicroBooNE reconstruction are not redundant, but rather complementary approaches that can be combined.

Results presented in this note are based on Pandora. However, to some extent, we expect results to be relevant to other paradigms as well. Indeed, higher level results are sensitive to the properties of the lower level inputs that are common to the other paradigms (waveforms or hits); in particular, the comparison of the reconstruction performance in data and Monte Carlo samples validates the accuracy of the common detector simulation.

The Pandora multi-algorithm pattern recognition takes place in two paths which share many of the same internal algorithms, but which have different objectives. The first path, called PandoraCosmic, is optimised for the reconstruction of cosmic-ray muons and their daughter delta rays. The second, PandoraNu, is instead optimised for the reconstruction of neutrino interactions and is performed on the subset of hits in the event that are not clearly associated with cosmic-ray activity [15]. The output of Pandora is organized in a hierarchy of reconstructed Particle Flow Particles (“PFParticles”), which describes the particle content in an observed event as a parent-daughter relationship chain. Final state PFParticles are classified as track-like or shower-like, and are associated with the corresponding track or shower object, a set of reconstructed 3D positions, and a reconstructed vertex position defining its interaction point or first energy deposit. A neu-

trino PFParticle can be created in the PandoraNu pass as part of the hierarchy, and represents the primary parent particle for a neutrino interaction [12].

The output of the Pandora pattern recognition is used as input for further higher level reconstruction algorithms, with the goal of providing measurements which are refined or complementary to the information from Pandora, or with the goal of performing a second-pass pattern recognition targeting specific topologies for which Pandora was not optimized. The higher level algorithms that are relevant for the present note are described in Sec. 2.1. The production of the samples used in these studies is described in Sec. 2.2.

## 2.1 Higher-level Reconstruction Algorithms

The main interest of this note is to measure the performance of reconstructing neutrino events in MicroBooNE data, and thus the focus is primarily on the output of the PandoraNu stage. To make this assessment, we further process the result from the PandoraNu stage to extract additional or refined information used in the analysis. Here, a brief description of the four specific algorithms used in the data-driven performance measurements is given.

### 2.1.1 Momentum measurement from Multiple Coulomb Scattering

The trajectory of charged particles in a medium is deviated due to electromagnetic scattering off atomic nuclei, a phenomenon commonly known as Multiple Coulomb Scattering (MCS). The RMS of the angular deviation distribution  $\sigma_0$  follows the Highland formula [16, 17]

$$\sigma_0 = \frac{S_2}{p\beta c} z \sqrt{\frac{\ell}{X_0}} \left[ 1 + \epsilon \ln \left( \frac{\ell}{X_0} \right) \right], \quad (1)$$

which depends on the particle’s momentum  $p$ , its relativistic term  $\beta$ , the thickness of the traversed layer  $\ell$ , and the radiation length of the target material  $X_0$ ; in the Particle Data Group definition [17]  $S_2$  and  $\epsilon$  are constants with values of 13.6 MeV and 0.038, respectively. For a given particle type and material, the particle momentum  $p$  can be estimated using the angular deviations along the trajectory; for most LArTPC experiments, this is the only method that can be used to estimate the momentum of particles exiting the detector. MicroBooNE developed a maximum likelihood fit based on a tuned Highland formula for argon [7] where, for  $\ell \equiv X_0 = 14$  cm,  $S_2$  is replaced with a momentum-dependent parameter  $\kappa(p) = (0.105 \text{ MeV}) / (p(\text{GeV}))^2 + 11.04 \text{ MeV}$ . This fit is performed on all Pandora tracks both in the forward and in backward direction; the likelihood is computed for momenta between 0.01 and 7.5 GeV in steps of 0.01 GeV, assuming a muon hypothesis. The resulting momentum estimate corresponds to the value that maximises the likelihood function. The comparison of the result under the two direction hypotheses can be used to probe the direction of the track and separate cosmic muons stopping in the detector from exiting muons produced in neutrino interactions.

### 2.1.2 Kalman filter fit of tracks

Tracks from Pandora feature three dimensional position and direction vectors at each hit; such vectors are estimated through a “sliding fit” procedure defined as follows. For  $x$  position values along the track, a linear fit in each plane is performed in the vicinity of such position; fits from two planes are projected in the 3rd plane, and the compatibility between the projection and the actual fit in the 3rd plane is evaluated with a  $\chi^2$ . The resulting position and direction are those

that minimize the  $\chi^2$  for all plane combinations. In order to refine the estimation of the track parameters and to extract their covariance matrix, tracks are further fitted with a Kalman filter procedure [18, 19]. Such a fit is initialized with parameters from the Pandora track under assumed large uncertainties. It then proceeds iteratively over all hits associated with the track: parameters are propagated to the plane defined by the wire containing the next hit and the drift direction  $x$ ; here they are updated with the hit measurement and then again propagated to the next hit. The propagation model is a straight line (as expected for a non-magnetized detector) and the propagated uncertainties account for MCS deviations. Uncertainties on the track parameters are constrained as more measurements are added along the fit. In order to solve ambiguities, the next hit is selected based on the minimum propagation distance; spurious hits are cleaned by requiring that the propagation distance is not opposite to the track direction. After all hits are processed in the forward direction, the fit is reversed and a Kalman filter smoothing step is performed in the backward direction so that the best estimate of parameters and uncertainties is evaluated at each point and especially at the track start.

### 2.1.3 Geometric fit of 3D vertex position

A first determination of the vertex position takes place during the PandoraNu pattern recognition stage, and is used to aid the reconstruction of tracks and showers emerging from the neutrino interaction point, as well as the identification of the particle hierarchy (i.e. “primary” products of the neutrino interaction, and “secondary” products from the decay or interaction of primaries in the detector).

The idea of the *Geometric3DVertexFitter* is to improve the vertex position measurement using the full information from reconstructed tracks, with the goal of augmenting the analysis selection and the association of tracks and showers to the vertex. The fitting algorithm proceeds as follows (see Fig. 3). Tracks fitted with the Kalman filter described above and associated with the daughters of the neutrino PFParticle are considered. At least two tracks are needed to perform the vertex fit. The two tracks with minimum distance between their start positions are first processed. The lines defined by the track start position and direction are considered, and the two points along the lines with minimum separation are found; the track uncertainties are respectively propagated to the two points, and the vertex (position and uncertainty) is computed as the average of the two points weighted by the corresponding uncertainties. In case there are more than two tracks, the remaining ones are sorted based on the higher number of hits and iteratively added with a similar weighted average procedure. If the impact parameter IP (defined as the distance between P and the vertex, where P is the point of minimum distance to the vertex along the start direction) of a given track is more than 3 times its uncertainty  $\sigma_{IP}$ , the track is discarded. Fitted vertices contain the following information: vertex position in 3D, the corresponding covariance matrix, and the vertex fit  $\chi^2$ . Also, for each track in the vertex the propagation distance, the IP, and the relative uncertainties are stored. The propagation distance is defined from the track start point to P; thus, it is expected to be negative or  $\sim 0$ ; a propagation distance significantly  $>0$  implies a vertex downstream the track start point and is a sign of reconstruction issues with the event. These features can be used in physics analyses to characterize the goodness of the vertex fit and to assess the compatibility of a track or a shower with the vertex.

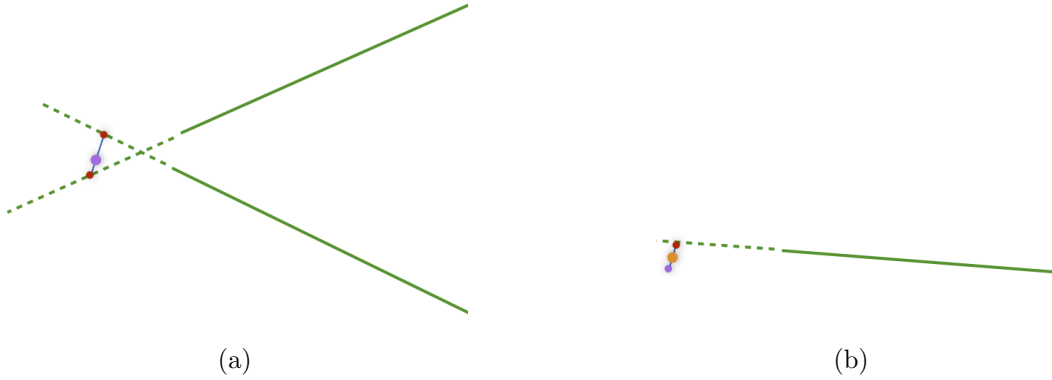


Figure 3: Sketch of the Geometric3DVertexFitter algorithm. Fit of two-track vertex: solid green lines represent the tracks in 3D, dashed green lines the extrapolations, red dots the minimum distance points, and the purple dot the vertex (a). Addition of the  $n$ -th track to the  $(n-1)$ -th track vertex, where the purple dot is the  $(n-1)$ -th track vertex and the orange dot is the final  $n$ -th track vertex (b).

#### 2.1.4 Shower reconstruction for photons from $\pi^0$ decays

The reconstruction of showers from photons originating from  $\pi^0$  decays is particularly challenging since the showers may be largely detached from the neutrino interaction vertex and, in neutrino interactions at BNB energies, many have energies below 100 MeV. In this energy range electrons shower in a stochastic fashion and may appear track-like in the readout (for a more detailed characterization of low energy electrons see ref. [6]). The reconstruction of electromagnetic showers performed in this study starts by examining the 2D clusters created by the Pandora pattern recognition algorithms in each readout plane. The linearity, hit dispersion and spatial extent of these clusters is examined to determine if they were induced by a track or a shower-like object. The hits designated as shower-like in this process are then clustered together using another clustering algorithm based on OpenCV, an open source image processing tool [20]. Hit positions in each wire plane are converted into polar coordinates around the reconstructed vertex position. As a first step, all contiguous hits are formed into a 2D cluster on a given plane. Then, nearby clusters that are approximately collinear are merged together using an iterative procedure in steps of about half a conversion length along the shower direction. Finally clusters are matched across wire planes based on their extent in the time coordinate. Matched clusters are used to compute various shower properties such as 3D direction and energy from the summed hit charge on the collection plane. The decisions made during the hit sorting stage coupled with the clustering produce showers with high purity, on average 92%, at the expense of completeness, on average 63%, which impacts the overall energy resolution of the showers. The individual shower reconstruction efficiency for photons coming from  $\nu_\mu + \text{Ar} \rightarrow \mu + \pi^0 + X$  interactions is on average 56% for all signal showers; showers above 300 MeV have a reconstruction efficiency consistent with 80%. A first estimate of the shower energy is obtained from the calibrated calorimetric information from the collection plane hits associated with the shower. Calibrations account for physical processes, detector, and electronics effects to convert the measured ADC values to the actual energy deposited [6]. Such effects include electronics gain, argon ionization, and ion recombination; in particular, given that electrons at these energies are approximately minimum ionizing particles, a constant recombination factor is used. This is the first fully automated reconstruction and selection of  $\pi^0$  decays with large scale LArTPC data.

## 2.2 Samples and Event Selection

MicroBooNE’s analysis work is organized around annual production campaigns of data and MC samples. Planned simulation and reconstruction improvements are integrated up to a given cutoff date when the sample production begins; the cutoff date is set such that large enough samples can be produced and analyzed in time for target conferences. The experiment code is part of LArSoft, the toolkit for simulation, reconstruction and analysis of LArTPC neutrino detectors [21].

The studies presented in this note are based on a data sample from the Fermilab Booster Neutrino Beam (BNB) corresponding to  $1.62 \times 10^{20}$  protons on target, after passing data and beam quality requirements [22], collected between February 2016 and July 2016. Neutrino interactions from the BNB are simulated using the GENIE neutrino generator [23], and cosmic interactions are simulated using the CORSIKA cosmic ray generator [24]. The particles generated by GENIE and CORSIKA are passed to Geant4 [25] where they are propagated through a simulated MicroBooNE detector. Data and simulation are then processed through the same reconstruction chain.

Unless otherwise stated, events in data and simulation are required to pass the following selection: a candidate  $\nu_\mu$ -induced  $\mu$  must have a deposited charge consistent with the spatial distribution of light collected on the PMT array during the trigger and a length,  $L$ , greater than 15 cm; this muon candidate is required to originate from a point within 3 cm of a 3D reconstructed vertex that is located within a fiducial volume taken as 10 cm from the up- and down-stream faces of the detector and 20 cm from the other sides. The muon candidate track is required to have an average hit charge consistent with a minimally ionizing particle and, to distinguish it from a mis-identified shower, no deflections greater than  $8^\circ$  are allowed along the track. To further reduce the cosmic contamination a set of requirements depending on the vertex multiplicity is applied; such cuts suppress topologies consistent with background from cosmic rays such as single tracks that exit the detector or are vertical, two-track vertices compatible with a muon decay into a Michel electron, and multi-track vertices with back-to-back track pairs. More details can be found in [26]. This event selection reduces the number of readouts containing only cosmic activity by 99.9%, creating a sample of events that is 80% pure in  $\nu_\mu$  charged current interactions. Given that the expected number of  $\nu_e$ -induced events passing the selection is negligible and provides no sensitivity to neutrino oscillation measurements (for which a blinded analysis is being developed), the  $1.62 \times 10^{20}$  (POT) sample is filtered according to this selection and made available to the collaboration for analyses.

### 3 Data-driven Performance Studies

#### 3.1 Momentum Measurement for Exiting Tracks

The MCS momentum fit described in Sec. 2.1.1 is used in various MicroBooNE analyses both for contained and exiting tracks, where tracks are defined to be contained if both ends are within the fiducial volume, and exiting otherwise. It is used as a tool for estimating the track momentum [15], as well as for rejecting cosmics by determining whether a track is a cosmic ray entering and stopping in the detector or a neutrino-induced muon exiting the detector. A previous MicroBooNE publication [7] demonstrated the performance of this algorithm in data for contained tracks only; such results are not directly applicable to exiting tracks since in the contained tracks case the fit is driven by the final part of the track, with lower momentum and larger scattering angles. Instead, in the exiting track case the final part of the track is missing, so that the momentum resolution is significantly worse. In this note, we thus study the performance for exiting tracks in data.

Working with contained tracks in data, the performance of the MCS fit was measured by comparing to the momentum derived with  $<4\%$  resolution from range-based methods. Such a method cannot be used directly to determine the momentum of exiting tracks, so we employ a different strategy to analyze the performance of exiting tracks in data. The basic scheme is to take a contained track in data and define a *pseudo-exiting* track by artificially removing some length from the end of the track to mimic the effect of exiting the TPC. In the MCS momentum fit, the track is split into segments with a nominal length of 14 cm, so we can create a pseudo-exiting track removing a certain number of segments from the end of a track; in this study, we look at 2, 4, and 6 segments removed. The performance of momentum measurement for exiting tracks will depend on two parameters: the true initial track momentum  $p_{\text{true}}$  and the track momentum when exiting the detector  $p_{\text{exit}}$ . In order to compute the bias and resolution for the MCS momentum measurement  $p_{\text{MCS}}$ , distributions of fractional inverse momentum difference  $(p_{\text{MCS}}^{-1} - p_{\text{true}}^{-1})/(p_{\text{true}}^{-1})$  in bins of true momentum are fit to Gaussian functions, where the mean of the fit determines the bias while the width of the fit determines the resolution for that bin (Fig. 4).

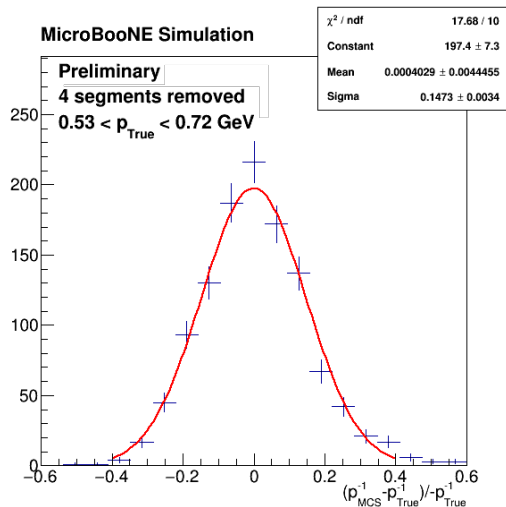


Figure 4: Example of distribution of fractional inverse momentum difference  $(p_{\text{MCS}}^{-1} - p_{\text{true}}^{-1})/(p_{\text{true}}^{-1})$  and the fit to derive the bias and the resolution of the MCS momentum measurement.

In the case of pseudo-exiting tracks,  $p_{\text{true}}$  can be approximated from the range-based momentum  $p_{\text{Range}}$  for the full (untruncated) track length, while  $p_{\text{exit}}$  is directly correlated with the removed

length at the end of the track and is approximately constant for a given number of removed segments. In this study, tracks in events passing the selection described in Sec. 2.2 are considered. The requirement of a minimum track length of 1 m is applied to all tracks, including pseudo-exiting tracks after segments are removed; this requirement also guarantees that the track sample is largely dominated by muons.

In order to validate the method, pseudo-exiting tracks with 4 segments removed are first compared to true exiting tracks in simulation. For this comparison, exiting tracks are required to match a simulated muon track which exits the detector with momentum  $0.22 < p_{\text{exit}} < 0.26$  GeV, corresponding to the momentum at the end of a pseudo-exiting track with 4 segments removed. As shown in Fig. 5, the agreement in bias and resolution for true exiting and pseudo-exiting tracks is rather good; there may be a small systematic difference in the resolution (Fig. 5b), but we consider this a minor effect and thus the method as validated. Similar tests are also performed for 2 and 6 segments removed, with similar conclusions.

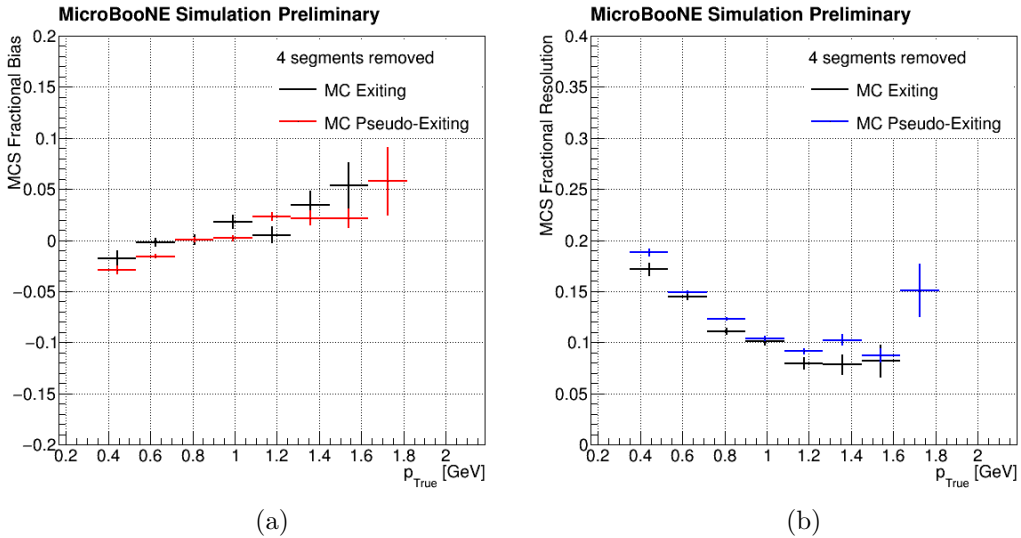
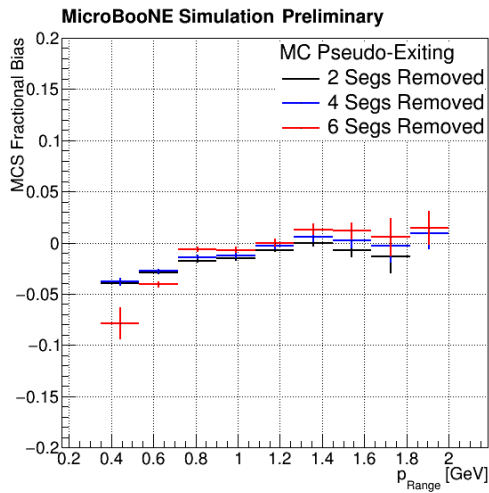
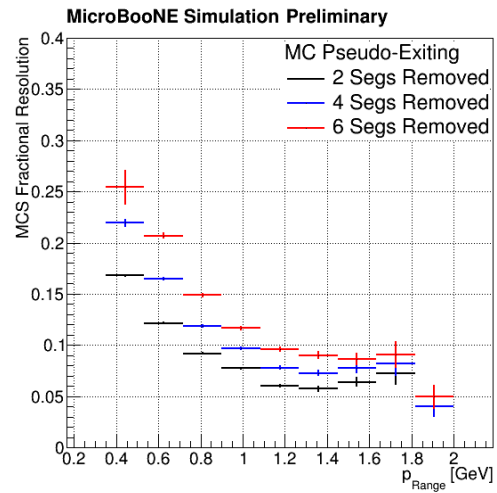


Figure 5: Comparison of MCS momentum bias (a) and resolution (b) vs. truth momentum for pseudo-exiting tracks with 4 segments removed and exiting tracks with  $0.22 < p_{\text{exit}} < 0.26$  GeV.

We then compare pseudo-exiting tracks in data to simulation, where bias and resolution of pseudo-exiting tracks are parametrized in terms of  $p_{\text{Range}}$ . As shown in Fig. 6, for 2, 4, and 6 segments removed the expected bias in simulation shows little variation, while the resolution degrades with a larger number of removed segments. The bias and resolution values observed in data for 2, 4, and 6 segments removed demonstrate a very good agreement with simulation (Fig. 7), thus validating in data the MCS momentum measurement for exiting tracks presented in ref. [7].

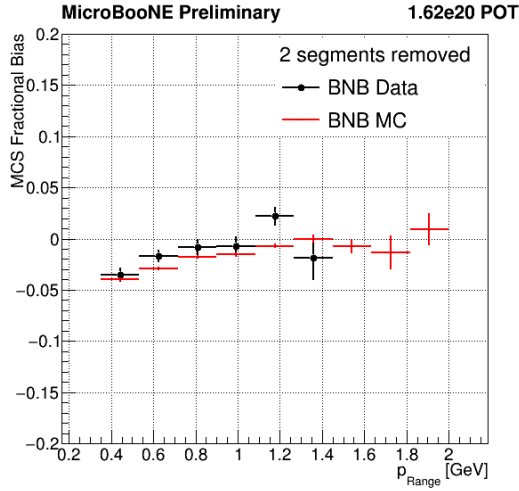


(a)

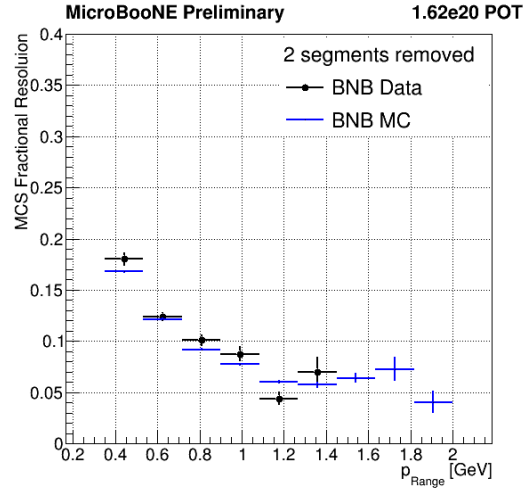


(b)

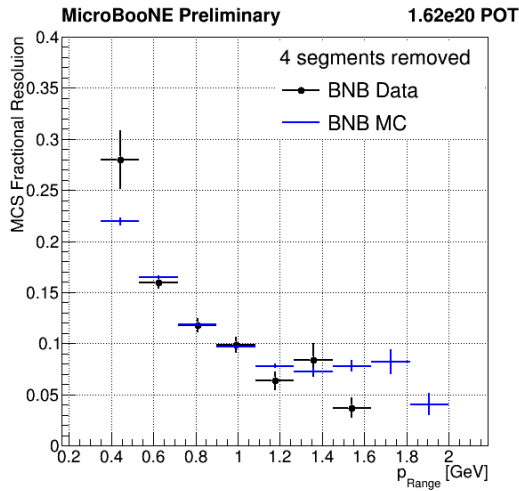
Figure 6: Comparison of MCS momentum bias (a) and resolution (b) vs. range-based momentum for pseudo-exiting tracks with 2,4,6 segments removed. The bias is similar for all numbers of removed segments, while the resolution degrades with larger number of removed segments.



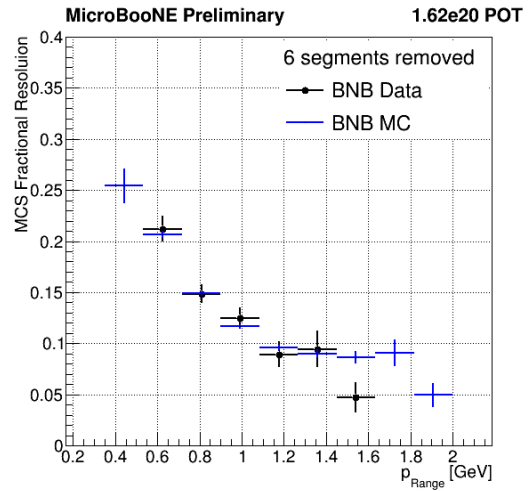
(a)



(b)



(c)



(d)

Figure 7: MCS momentum performance for pseudo-exiting tracks in data compared to simulation: bias for 2 segments removed (a) and resolution for 2 (b), 4 (c), and 6 (d) segments removed.

## 3.2 Track Position and Direction Resolution

Assessing the track resolution in data is crucial for the understanding of the detector, event reconstruction, and selection, which are necessary in order to validate physics analyses. A track resolution measurement directly probes the detector technology performance, where the space resolution is expected to be driven by the wire spacing, the readout clock frequency, drift properties of the medium and electronic effects in the signal readout. As a consequence, track resolution measurements are sensitive to various lower-level detector effects and act as a robust test of their implementation in simulation. Track and vertex position resolutions drive analysis-level selections, for instance requiring the track start position to be within a maximum distance from the vertex [27]; also, good modeling of the track direction resolution is important for differential cross sections measurements as a function of the track direction [15].

Neutrino interactions in LArTPC detectors do not offer many handles to constrain the reconstruction performance using resonances or high precision external taggers; therefore a reference measurement for extracting the resolution needs to be defined from the LArTPC measurement itself by splitting a track to create two disjoint hit sets. The two hit sets are then fit independently to produce two *split tracks*. Both split tracks are projected to the same plane, and the difference between a measured track parameter  $k$  from the two split tracks ( $k_{\text{ST1}} - k_{\text{ST2}}$ ) is plotted. In case the two split tracks are uncorrelated, the width of the distribution will be  $\sqrt{\sigma_{k,\text{ST1}}^2 + \sigma_{k,\text{ST2}}^2}$  (where  $\sigma_{k,\text{ST}i}$  is the resolution for the parameter  $k$  from split track  $i$ ). If  $\sigma_{k,\text{ST1}} = \sigma_{k,\text{ST2}} \equiv \sigma_{k,\text{ST}}$ , the width of the distribution will be  $\sqrt{2}\sigma_{k,\text{ST}}$ , so that the resolution  $\sigma_{k,\text{ST}}$  can be estimated as the width divided by  $\sqrt{2}$ .

Split tracks need to be defined in such a way that they are uncorrelated, and that they have the same resolution (at least approximately). Various ideas can be explored, but the two simplest are splitting the hit set by even vs odd wire number and splitting the hit set upstream or downstream of the middle point. The even vs odd method is not guaranteed to produce two uncorrelated tracks for two reasons: first, deviations in the trajectory due to MCS will be correlated in the two hit sets, and, second, the signal in nearby wires might be correlated. In this study tracks are split in an “upstream” and a “downstream” segment, defined as follows (see also Fig. 8). The hit set from a PandoraNu track fitted with the Kalman filter described in Sec. 2.1.2 is divided into three subsets based on the middle point hit along the track direction: upstream, downstream, and *the gap*. Apart from those in the gap, hits on the side of middle point towards the track start go in the upstream set, those towards the end go in the downstream set. The gap consists of a buffer of 10 hits on each side of the middle point hit, and is designed to make sure there are no inter-wire signal correlations between hits in the other two sets. The upstream and downstream hit sets are fit independently using the same Kalman filter-based procedure as the original track, and parameters are compared at the middle point of the original track.

Resolutions are expected to vary as a function of various properties of the track: the particle type, its momentum, the number of hits used in the track fit, the presence of detector problems (e.g. dead wires) in the proximity of the track. In order to avoid contaminations of multiple types, we select a sample of exiting tracks which is largely dominated by muons. We choose to primarily characterize the resolution in terms of the momentum, for a few reasons: it is correlated with the number of hits and the track length, and it allows to identify a high-momentum region where the effect of MCS is negligible, thus probing the detector technology performance. The momentum is measured with the likelihood fit of the MCS angular deviations along the original track  $p_{\text{MCS}}^\mu$  (described in Sec. 2.1.1). The second parametrization we present is with respect to the global cartesian coordinate  $z$ , so that it is possible to check the effect of dead wire regions on the

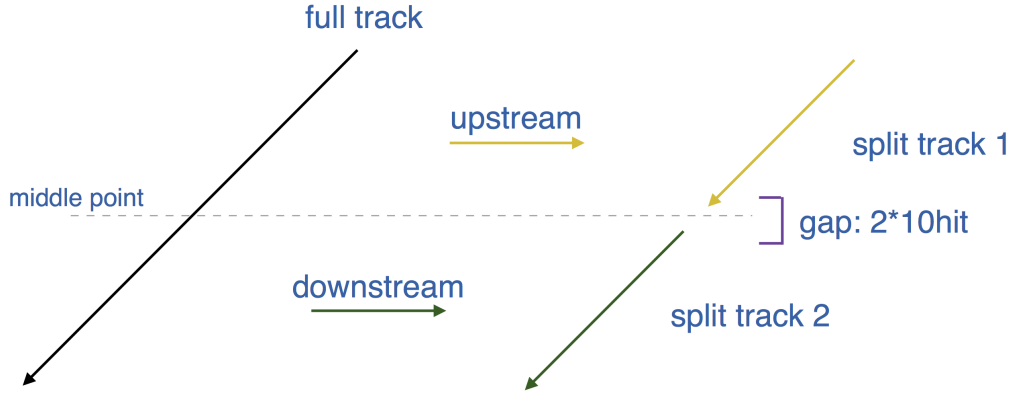


Figure 8: Sketch of the method to split tracks at the middle point.

resolution.

In order to further remove cosmic contamination, in addition to the event selection described in Sec. 2.2, we require at least 2 tracks associated with the neutrino vertex and with vertical direction  $|u_y| < 0.6$ . Resolutions obtained in MC samples with and without simulated cosmic background show negligible differences after applying these cuts.

One relevant question is how closely the resolution obtained with the split track method approximates the resolution of the full track at the interaction vertex. Differences may arise due to the fact that in the split track case about half of the hits are used, that at the middle point the actual momentum is lower than the one at the start, and that resolutions at the midpoint are not sensitive to issues related to other vertex activity. The main similarities are that in both cases the fit estimates the track parameters using hits only from one side, that the same detector effects affect both definitions (e.g. drift distance, dead wires), and that, for high enough momentum, split tracks achieve the same resolution values as full tracks at the vertex (Fig. 9). In summary, while split tracks are unavoidably different from full tracks, they probe a resolution definition that is reasonably close to the one of interest for physics analyses and it is fair to assume that the level of data-MC agreement observed for split tracks at the midpoint can, to a large degree, be applied to full tracks at the vertex.

Results as a function of  $p_{\text{MCS}}^\mu$  (Fig. 10) show in general a good data-MC agreement, typically within 10%. The  $y$  position resolution appears to be systematically worse in data up to the 20% level; this parameter is mostly constrained by measurements in induction planes, where wires are tilted with respect to the vertical direction, so this disagreement may indicate issues at the signal processing level for induction planes—for instance, the 2D deconvolution described in [9] was not used yet in the current production campaign and will improve the data-MC agreement. It is also interesting to see that the position resolution at high momentum reach levels close to the expected values based on the detector properties, and in particular go below the millimeter level as outlined in the MicroBooNE TDR [28]. Results parametrized vs  $z$  position (Fig. 11) show a similar level of agreement, and in particular demonstrate that the data-MC agreement does not deteriorate in the detector regions at  $z < 400$  cm and  $z \sim 700$  cm which are affected by shorted wires.

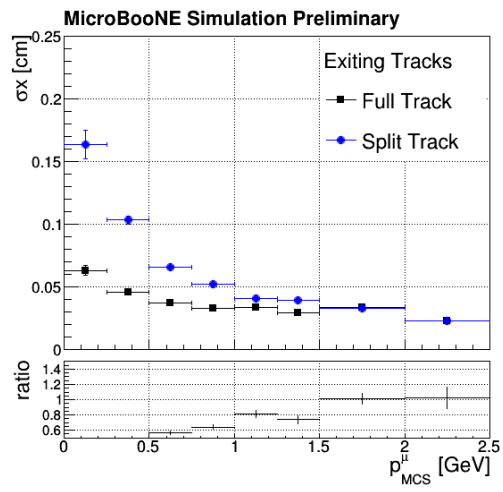
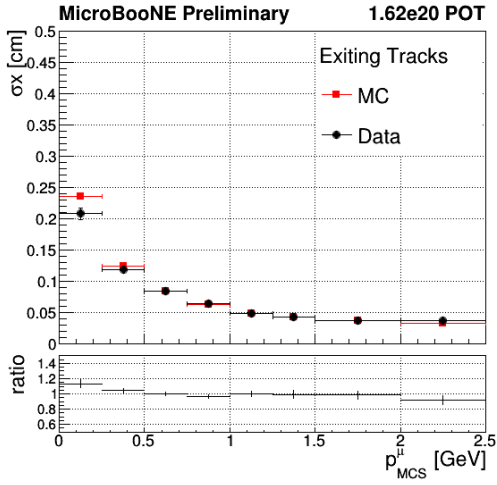
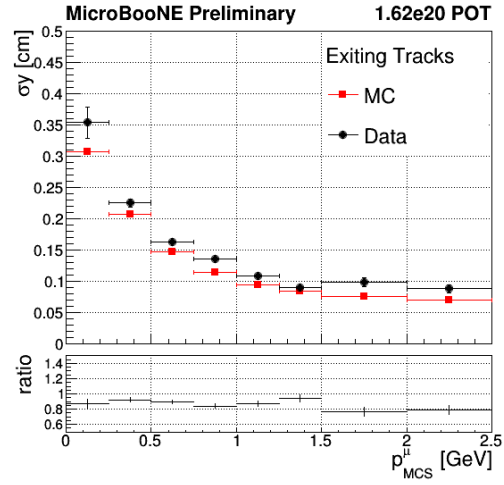


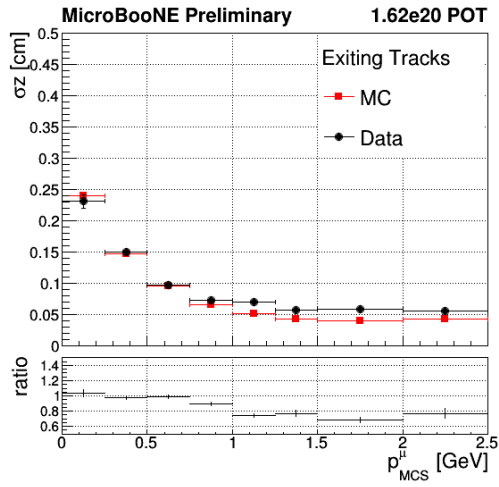
Figure 9: Position resolution in the  $x$  coordinate for full tracks at the vertex and split tracks at the midpoint of the full track. Resolutions are obtained comparing the track reconstructed position to the simulated one.



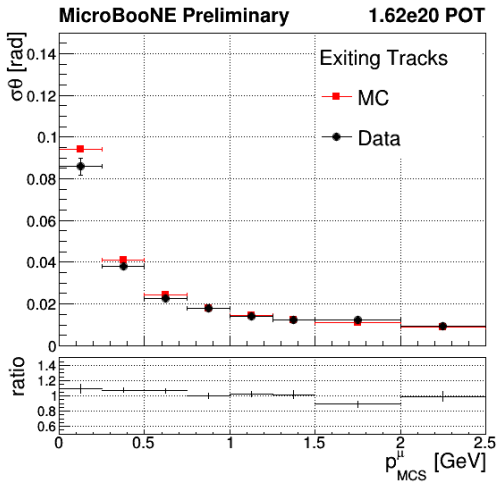
(a) x position



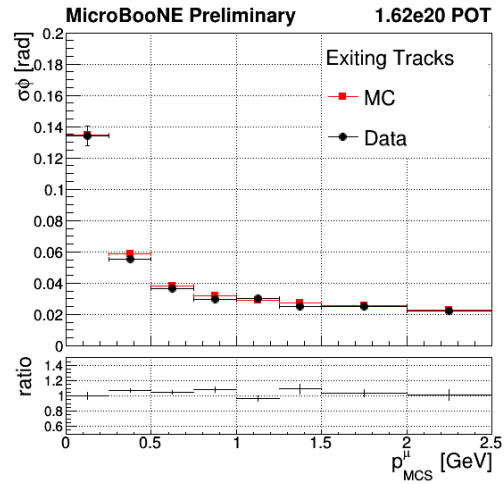
(b) y position



(c) z position

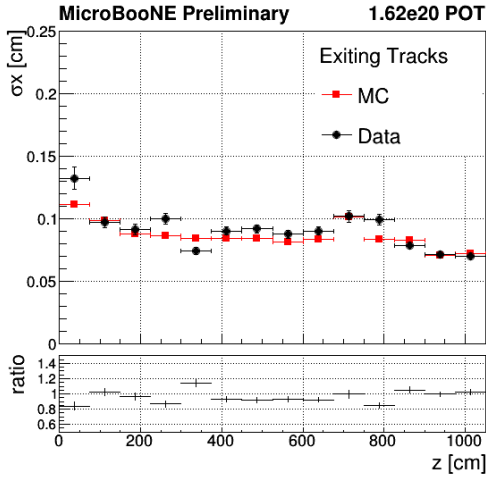


(d)  $\theta$  direction

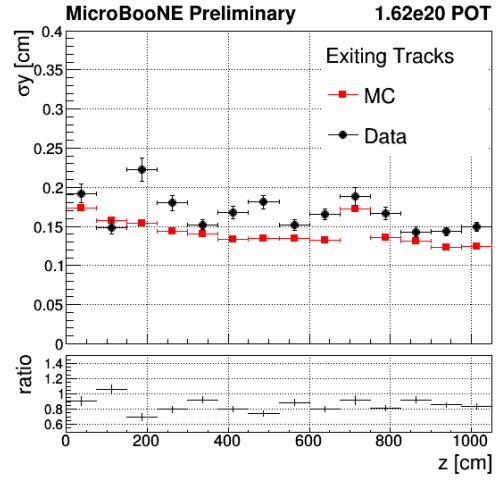


(e)  $\phi$  direction

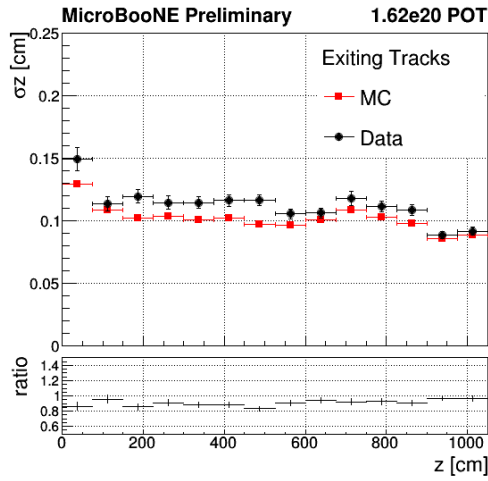
Figure 10: Split track data-driven resolution vs MCS momentum for exiting tracks. Resolutions are defined at the track middle point using the procedure outlined in the text. Comparisons are shown between simulation and data.



(a) x position



(b) y position



(c) z position

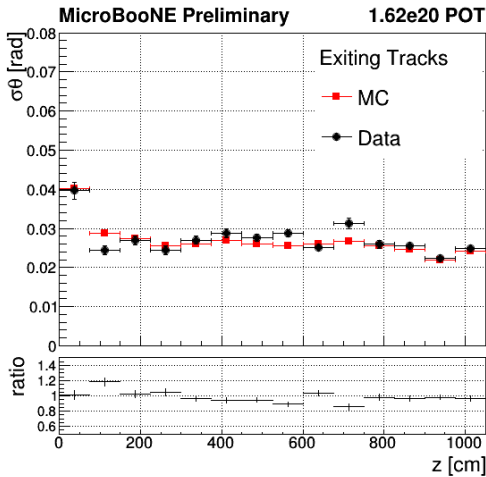
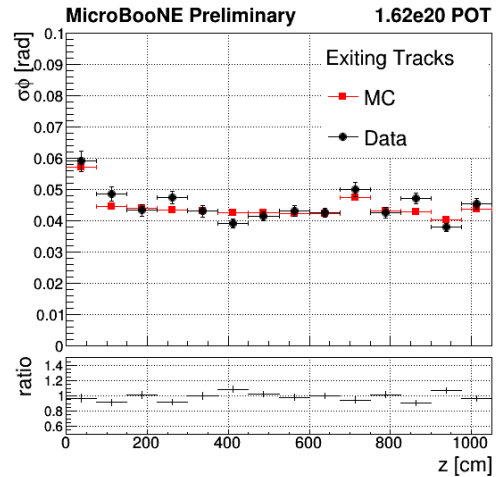
(d)  $\theta$  direction(e)  $\phi$  direction

Figure 11: Split track data-driven resolution vs  $z$  position for exiting tracks. Resolutions are defined at the track middle point using the procedure outlined in the text. Comparisons are shown between simulation and data.

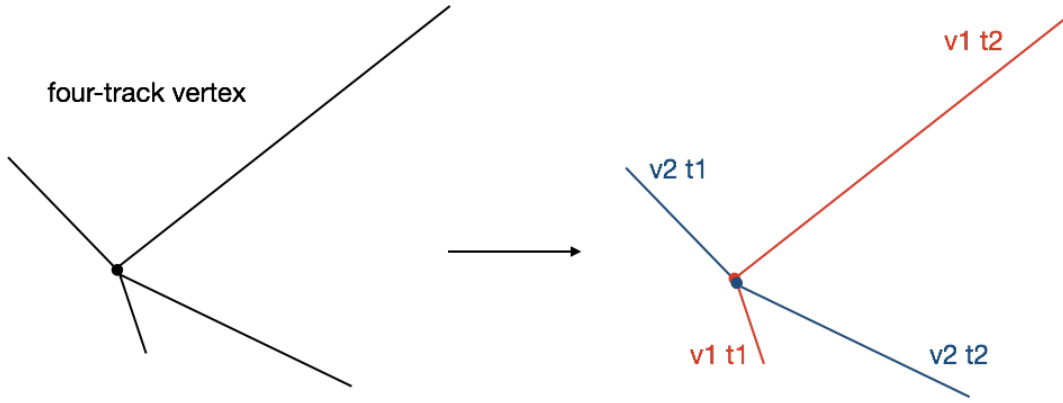


Figure 12: Illustration of the Split Vertex method.

### 3.3 Vertex Resolution

An accurate evaluation of the vertex position resolution in data is a critical test of the reconstruction performance. Track and vertex resolutions are the driver for analysis-level selections where the compatibility of a track with a given vertex is probed. Additionally, a precise vertex determination is a key to proper event reconstruction (see e.g. Sec. 2.1.4). Finally, a vertex fitting algorithm such as the Geometric3DVertexFitter (see Sec. 2.1.3) is a good validation test for a high-level usage of reconstructed tracks.

We measure the vertex resolution in data using the following method. First, vertices from Geometric3DVertexFitter where exactly four tracks have been used in the fit are selected. The four tracks are then split in two sets:  $v_1$ , which includes the shortest and longest track, and  $v_2$ , which includes the other two. Each set is then independently fit with the Geometric3DVertexFitter, and the resolution of a two-track vertex is extracted from the comparison of the positions from the two “split vertices”  $v_1$  and  $v_2$  (Fig. 12). Assuming that the two split vertices have the same resolution, it can be evaluated as the width of the difference between the  $v_1$  and  $v_2$  positions divided by the square root of two.

Four-track vertices are a rare event in MicroBooNE data. Neutrino interactions at BNB energies are dominated by lower multiplicity vertices due to quasi-elastic interactions and resonance production. Cosmic rays are not expected to produce genuine four-track vertices, but in rare occasions they can fake this topology, for instance in the case of reconstruction problems or in the presence of “crossing tracks”, i.e. tracks at different times, but producing ionization electrons that arrive in coincidence at the anode.

The data sample considered in this study corresponds to about  $5 \times 10^{19}$  protons on target. In order to keep the efficiency high for neutrino-like topologies, only a minimal event selection, looser than the one described in Sec. 2.2, is applied; nevertheless, we verify that the selected topologies in data are typically consistent with those from neutrino interactions. This selection requires that the event passes the data and beam quality requirements [22] and that a vertex with exactly four associated tracks according to the fitter is found. The basic properties of split vertices are studied in simulated events. The track length and the number of valid trajectory points in the track are first considered:  $v_1$  consists typically of a very long track (mean of 116 cm and 440 hits) and a very short one (12 cm and 20 hits), while the two tracks in  $v_2$  tend to be more similar (50 and 20 cm, 170 and 55 hits respectively). Next, the propagation distance (as defined in Sec. 2.1.3) and the impact parameter significance  $IP/\sigma_{IP}$  are studied: distributions follow the expected behavior and are rather similar for  $v_1$  and  $v_2$ . To assure a good control of the resolution, but at the same

time avoiding to limit too much the number of selected vertices, the following list of cuts is defined on top of the preselection: track length greater than 2 cm, at least 8 hits, propagation distance greater than -5 cm and less than 2 cm, and  $IP/\sigma_{IP} < 1$ . Only vertices for which all tracks pass this selection are considered. In addition, to suppress the topology where two crossing cosmic rays are split into two pairs of back-to-back tracks, all combinations of track pairs in the original four-track vertices are required to have azimuthal angle difference  $\Delta\phi$  less than 3.1 or larger than 3.2 rad.

To validate this method for determining the vertex resolution in data we compare the truth-based resolutions for  $v_1$  and  $v_2$  with the resolution from the data-driven method. Figure 13 demonstrates that, despite the different track lengths, the resolutions from  $v_1$  and  $v_2$  are compatible; the data-driven resolution is very close to the truth-based values, proving that the method is valid.

Figure 14 shows results in data for the three cartesian coordinates and a comparison of the extracted resolution in simulation is presented in Table 1. The data sample consists of only 71 events, so the statistical uncertainties in the data results are typically large (10-20%). The agreement between data and MC in terms of resolution is rather good: differences are within uncertainties, even if data tends to be slightly worse than MC. Moving forward, this study will need to be repeated with a larger data sample so that, on the one hand, statistical uncertainties can be reduced and, on the other hand, more stringent cuts can be applied to probe the best achievable performance.

Table 1: Numerical results of vertex resolutions in data and MC as obtained with the split vertex method.

Resolution	Data	MC
$x$	$0.15 \pm 0.02$ cm	$0.133 \pm 0.005$ cm
$y$	$0.24 \pm 0.05$ cm	$0.182 \pm 0.006$ cm
$z$	$0.18 \pm 0.02$ cm	$0.209 \pm 0.009$ cm

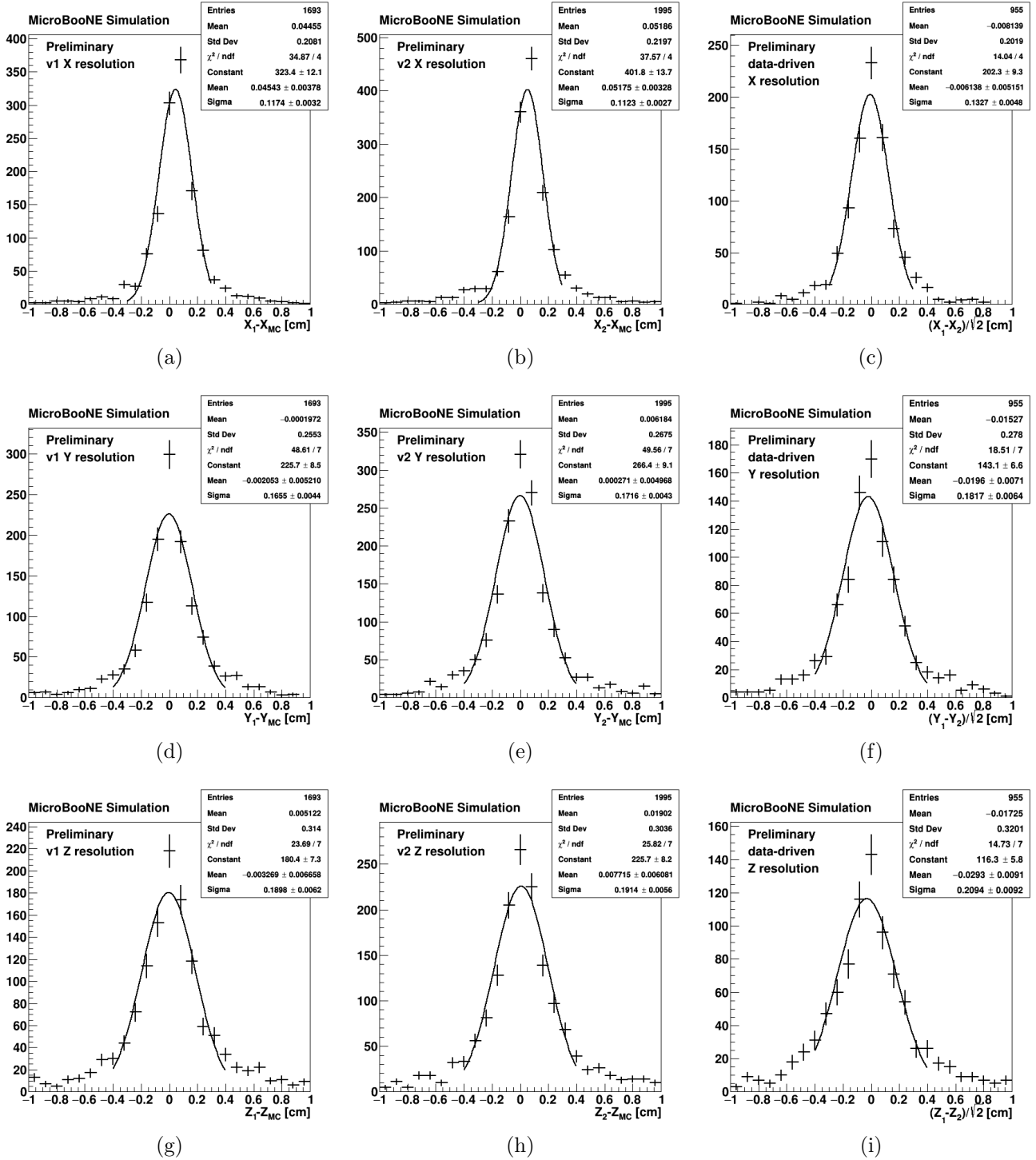


Figure 13:  $x$ ,  $y$ ,  $z$  vertex position resolution in MC. Left: truth-based resolution for  $v_1$ ; middle: truth-based resolution for  $v_2$ , right: data-driven resolution. Distributions are fitted with a Gaussian, and the resolution is estimated as the fitted width. Even ignoring the tails, a single Gaussian does not fit the distributions well in all cases, but nevertheless it can be used to give a relative measure of the width of the distributions.

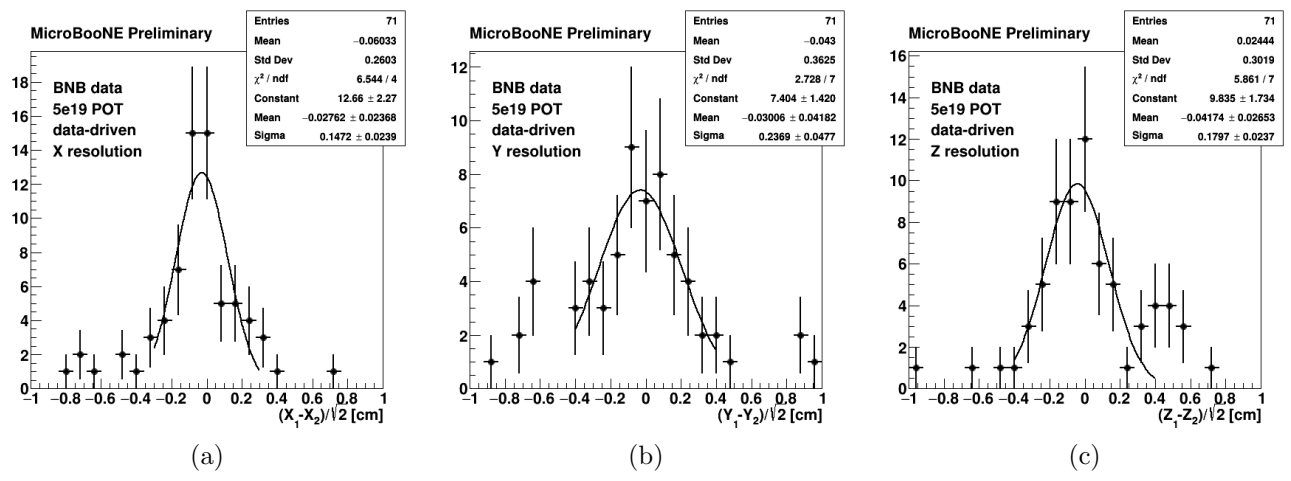


Figure 14: Data-driven  $x$ ,  $y$ ,  $z$  vertex position resolutions in data. The split vertex method has been used as described in the text.

### 3.4 Shower Energy Corrections and $\pi^0$ Mass Peak Reconstruction

In this study, a set of shower energy corrections, derived on simulation, is applied to diphoton events in data to prove that fully automated shower reconstruction in MicroBooNE is able to identify photons from  $\pi^0$ . This procedure has been employed in the context of the cross section measurement for  $\pi^0$  production in  $\nu_\mu$  charged current (CC) interactions [26].

First, events compatible with  $\nu_\mu$  CC interactions are selected with the requirements described in Sec. 2.2; in the selected events, a second-pass shower reconstruction is performed as described in Sec. 2.1.4. Reconstructed showers include a first energy estimate  $E_{\text{uncorr}}$ , which already accounts for detector calibrations. At this stage,  $E_{\text{uncorr}}$  shows a bias with respect to the true deposited energy resolution on the order of 30% in the peak, with a long tail towards larger amounts of missing energy. The population of showers that are reconstructed with more energy than what was deposited is negligible compared to the opposite, and results from showers that overlap with uncorrelated detector activity. Throughout the rest of this study we will focus on the sources of energy loss and neglect the source of energy gains.

The impact of this energy bias is evaluated in data using the standard candle provided by the  $\pi^0$  mass peak. Shower pairs are selected requiring that the two showers have an impact parameter of less than 4 cm, that the two showers have a 3D opening angle greater than 0.35 rad, that the leading shower has  $E_{\text{uncorr}} > 40$  MeV, and that the leading and subleading shower start less than 80 cm and 100 cm away from the vertex, respectively. In particular, the opening angle requirement assures that the two shower clusters are well separated so that the probability for inter-shower contaminations is suppressed. Fig. 15 shows the invariant mass of the selected shower pairs in data and simulation; we can observe that the data peak has an average value that is significantly offset relative to the expected neutral pion mass of 134.98 MeV.

The source of this off-set is primarily due to energy being missed in the clustering and reconstruction of the showers; a significant mis-reconstruction of the photon angles is excluded since it would contribute to a high mass tail which is not observed; furthermore, MC studies demonstrate an angular resolution of order 5 degrees. To address these energy losses, energy corrections are derived in simulation, where the reconstructed shower is required to be matched to a true photon from a  $\pi^0$  decay from a neutrino interaction. The sources of energy loss can be broken down into two classes: (1) losses due to the hit-sorting and clustering scheme and (2) energy depositions being below the hit finding threshold. Additional losses may be due to partial containment (deposited energy is measured in the active TPC volume), energy falling on non-responsive channels, and energy being deposited in regions with non-standard responses. These effects, integrated across the full detector volume, are small compared to the effects enumerated above; nevertheless, they may play a significant role in specific regions of the detector and may be addressed in future work.

The first correction we derive corresponds to the inefficiencies of the clustering methods. This correction is specific to the reconstruction approach used in this study, but a similar procedure can be used to derive a correction for other reconstruction techniques. To derive a correction we begin with the true simulated showers that reconstructed showers are matched to. We then look for all the reconstructed hits which these showers contributed the most energy to, and cluster these hits together; showers obtained with this procedure are named *perfectly clustered showers*. Hits in perfectly clustered showers utilize the same calorimetric constants applied in the shower reconstruction, so we expect the main difference in terms of energy to be only related to hits not being associated with reconstructed showers. To generate a correction we plot the reconstructed shower energy against the perfectly clustered shower energy, as shown in Fig. 16, and profile this 2D distribution in the perfectly clustered shower energy (red histogram). The profile histogram

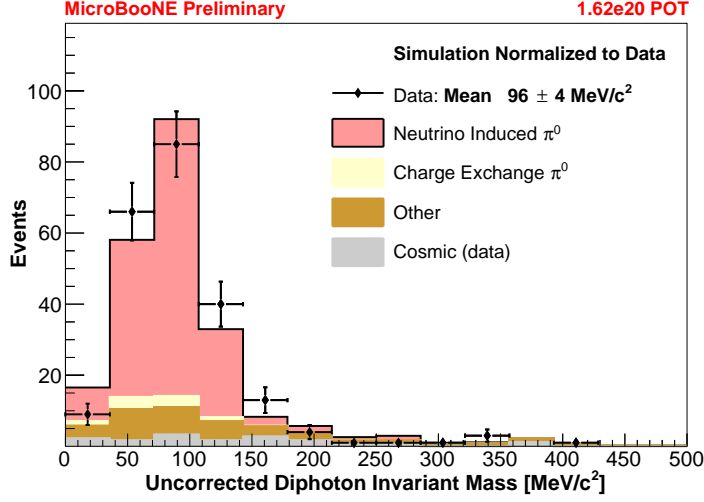


Figure 15: Invariant mass of selected dishower events, where the shower energy is not corrected. The reported mean value is the average of all data entries. At this stage the  $\pi^0$  mass peak appears significantly shifted towards lower values than the true  $\pi^0$  mass. See the text for details about the selection.

plots the mean reconstructed shower energy in that bin of perfectly clustered shower energy with the uncertainty on that mean. The shower energy corrected for clustering effects is defined as the inverse of the linear fit to the profile histogram:

$$E_{\text{clust}}^C = (E_{\text{uncorr}} - 7.9 \text{ MeV})/0.68. \quad (2)$$

The clustering correction factor appears to be relatively large, and this is a consequence of the fact that the shower reconstruction was optimized for purity, on average 92%, over completeness, on average 64%, to address different sources of shower contamination (see Sec. 2.1.4).

The next largest effect to the shower energy is the deposited charge that is not reconstructed as hits. This happens due the thresholds present in the hit-finding procedures. We can study the impact of this by comparing the perfectly clustered shower energy to the true deposited energy, the energy that the particle deposits in the active TPC volume in Geant4. The comparison of these two energies can be found in Fig. 17. A linear fit to the most probable value of the fraction of deposited energy that ends up in the perfectly clustered shower is performed in bins of perfectly clustered shower energy. This function shows a very small energy dependent correction, and can be used to define a correction to the cluster-corrected shower energy due to hit thresholding:

$$\frac{E_{\text{hit}}^C}{E_{\text{clust}}^C} = 1.05 + (1.5 \times 10^{-4} \text{ MeV}^{-1})E_{\text{clust}}^C. \quad (3)$$

Combining these two corrections, a total correction accounting for the two main sources of energy loss, can be obtained (Fig. 18). To do this we first apply the correction for the clustering, Eq. 2 which, on average, brings the shower energy closer to perfectly clustered shower energy. Next, we can correct the result for the energy that was not converted into hits by applying Eq. 3. With respect to the actual deposited energy, these corrections move the average bias  $\langle (E_{\text{reco}} - E_{\text{dep}})/E_{\text{dep}} \rangle$  from -34% for  $E_{\text{reco}} = E_{\text{uncorr}}$  to -15% for  $E_{\text{reco}} = E_{\text{clust}}^C$ , and then to -9% for  $E_{\text{reco}} = E_{\text{hit}}^C$ . The fact that, even after the second correction, the average bias is negative is due to the asymmetric nature of these distributions so that bringing the average bias to  $\sim 0$  would move the majority of events to a larger positive bias.

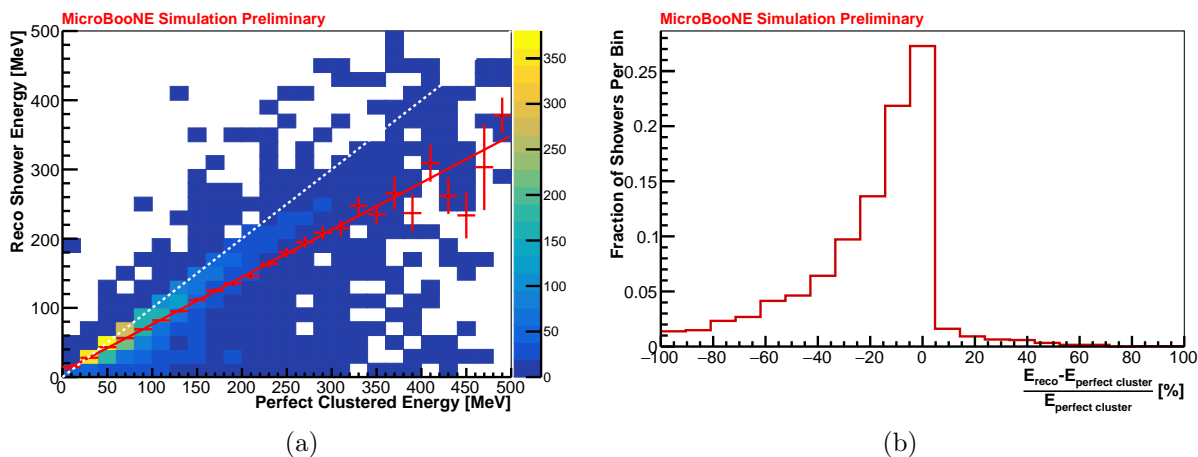


Figure 16: Comparison of the perfectly clustered shower energy to the reconstructed shower energy for reconstructed showers that can be associated back to true photons originating from  $\pi^0$  produced in neutrino interactions. Plotted on top of the 2D distribution (a) is a profile histogram of the mean value of reconstructed shower energy in each bin of perfect clustered energy with the uncertainty on the mean. A linear fit of the profile histogram is also included (solid red line). The fractional difference between the uncorrected reconstructed and the perfectly clustered energy is also shown (b).

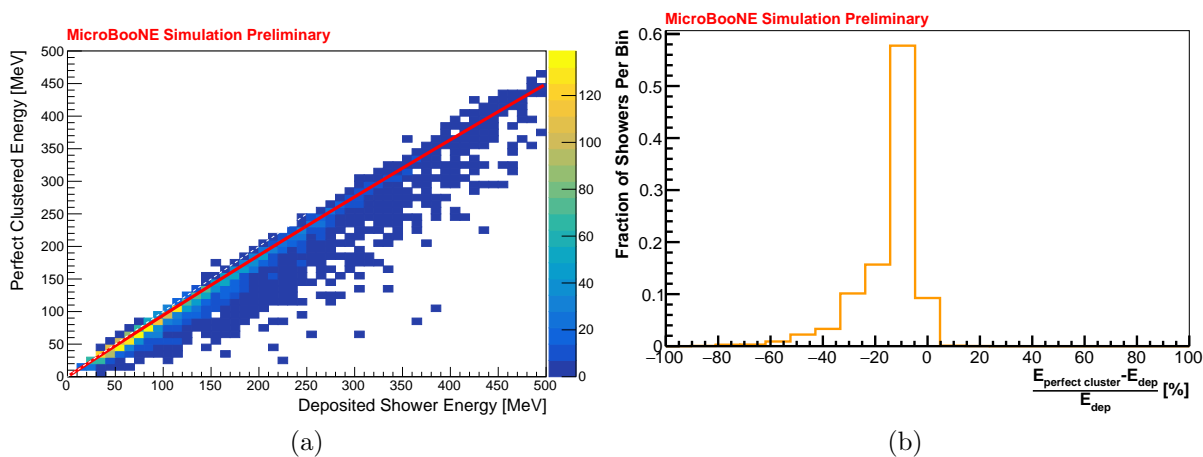


Figure 17: A comparison of the perfectly clustered shower energy and the true deposited energy of the shower. Plotted on top of the 2D distribution (a) is a linear fit to the most probable value of the fraction of deposited energy that ends up in the perfectly clustered shower (solid red line). The fractional difference between the perfectly clustered and the simulated deposited energy is also shown (b).

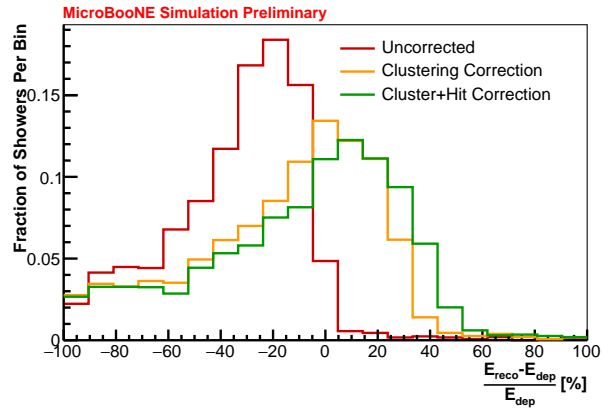


Figure 18: Fractional difference of shower energies at different correction stages with respect to the simulated deposited energy. The uncorrected shower energy is significantly biased to lower energy values. The subsequent clustering and hit thresholding corrections bring the average corrected energy close to the simulated values; note that, due to the tail, this correction strategy results in an overcorrection for the most probable value.

After applying these corrections on a shower-by-shower basis we can plot the corrected diphoton mass, shown in Fig. 19. We find that the average mass distribution has shifted to  $(128 \pm 5)$  MeV, and is now close to the expectation of the neutral pion mass; at the same time, it has also broadened given that we are correcting for the average missing clustered shower energy which leads to both over-corrections and undercorrections. When the resulting distribution is fitted with a Gaussian plus a linear function, where the linear function accounts for the non- $\pi^0$  backgrounds, we find that the peak of the Gaussian sits at  $(126 \pm 11)$  MeV, within uncertainties of the expected neutral pion mass.

This study demonstrates that MC-driven corrections applied to data are able to restore the expected  $\pi^0$  mass value, thus proving that the clustering performance as well as hit thresholds are not too far off in simulation with respect to what observed in data. As already noted, the largest correction (and thus the largest impact of the resolution) is due to clustering effects, so significant improvements are expected after upgrades to the clustering technique are included in the reconstruction. Nevertheless, as shown in ref. [26], the performance of the shower reconstruction presented here already reaches levels comparable to expectations from the DUNE CDR [3].

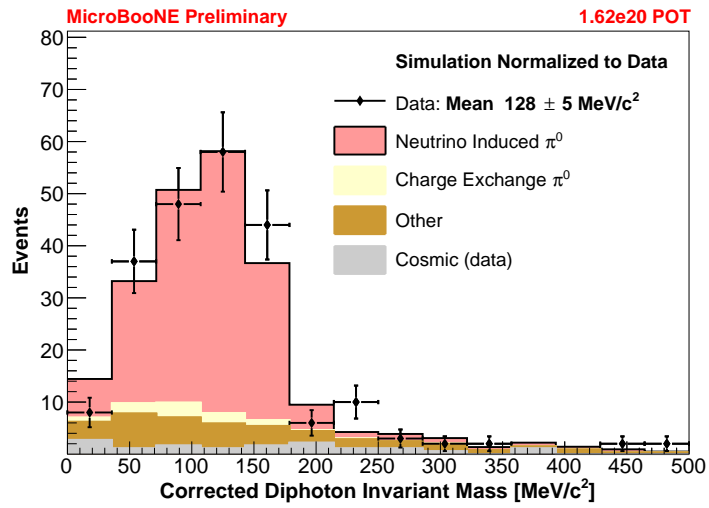


Figure 19: A data to MC comparison of the  $\pi^0$  mass peak across the full Run 1 data set after correcting the shower energy for clustering and hit thresholding effects. The reported mean value is the average of all data entries. See the text for details about the selection.

## 4 Conclusions

We have presented a set of performance measurements relative to the reconstruction of tracks, showers, and vertices in MicroBooNE data which are in good agreement with predictions from simulations. The achieved level of performance is satisfactory for the purpose of analyses presented at conferences in summer 2018; nevertheless, based on current known limitations, plans for further improvements are underway. The techniques presented here have a broader validity than MicroBooNE and could be applied to other LArTPC detectors that will turn on in the next months or years.

## Acknowledgements

We acknowledge the support of the Fermi National Accelerator Laboratory (Fermilab). Fermilab is managed by Fermi Research Alliance, LLC (FRA), acting under Contract No. DE-AC02-07CH11359. MicroBooNE is supported by the following: the U.S. Department of Energy, Office of Science, Offices of High Energy Physics and Nuclear Physics; the U.S. National Science Foundation; the Swiss National Science Foundation; the Science and Technology Facilities Council of the United Kingdom; and The Royal Society (United Kingdom). Additional support for the laser calibration system and cosmic ray tagger was provided by the Albert Einstein Center for Fundamental Physics, Bern, Switzerland.

## References

- [1] MicroBooNE Collaboration, R. Acciarri *et al.*, “Design and Construction of the MicroBooNE Detector,” *JINST* **12** no. 02, (2017) P02017 FERMILAB-PUB-16-613-ND, [arXiv:1612.05824 \[physics.ins-det\]](#).
- [2] LAr1-ND, ICARUS-WA104, MicroBooNE Collaboration, M. Antonello *et al.*, “A Proposal for a Three Detector Short-Baseline Neutrino Oscillation Program in the Fermilab Booster Neutrino Beam,” [arXiv:1503.01520 \[physics.ins-det\]](#).
- [3] DUNE Collaboration, R. Acciarri *et al.*, “Long-Baseline Neutrino Facility (LBNF) and Deep Underground Neutrino Experiment (DUNE),” FERMILAB-DESIGN-2016-04, [arXiv:1601.02984 \[physics.ins-det\]](#).
- [4] MiniBooNE Collaboration, A. A. Aguilar-Arevalo *et al.*, “Unexplained Excess of Electron-Like Events From a 1-GeV Neutrino Beam,” *Phys. Rev. Lett.* **102** (2009) 101802 FERMILAB-PUB-08-570, LA-UR-08-07142, [arXiv:0812.2243 \[hep-ex\]](#).
- [5] MicroBooNE Collaboration, R. Acciarri *et al.*, “Measurement of cosmic-ray reconstruction efficiencies in the MicroBooNE LArTPC using a small external cosmic-ray counter,” *JINST* **12** no. 12, (2017) P12030 FERMILAB-PUB-17-213-ND, [arXiv:1707.09903 \[hep-ex\]](#).
- [6] MicroBooNE Collaboration, R. Acciarri *et al.*, “Michel Electron Reconstruction Using Cosmic-Ray Data from the MicroBooNE LArTPC,” *JINST* **12** no. 09, (2017) P09014 FERMILAB-PUB-17-090-ND, [arXiv:1704.02927 \[physics.ins-det\]](#).

- [7] MicroBooNE Collaboration, P. Abratenko *et al.*, “Determination of muon momentum in the MicroBooNE LArTPC using an improved model of multiple Coulomb scattering,” *JINST* **12** no. 10, (2017) P10010 FERMILAB-PUB-17-076-ND, arXiv:1703.06187 [physics.ins-det].
- [8] MicroBooNE Collaboration, R. Acciarri *et al.*, “Noise Characterization and Filtering in the MicroBooNE Liquid Argon TPC,” *JINST* **12** no. 08, (2017) P08003 FERMILAB-PUB-17-163-ND, arXiv:1705.07341 [physics.ins-det].
- [9] MicroBooNE Collaboration, C. Adams *et al.*, “Ionization Electron Signal Processing in Single Phase LArTPCs I. Algorithm Description and Quantitative Evaluation with MicroBooNE Simulation,” FERMILAB-PUB-18-056-ND-PPD, arXiv:1802.08709 [physics.ins-det].
- [10] MicroBooNE Collaboration, C. Adams *et al.*, “Ionization Electron Signal Processing in Single Phase LArTPCs II. Data/Simulation Comparison and Performance in MicroBooNE,” FERMILAB-PUB-18-096-ND, arXiv:1804.02583 [physics.ins-det].
- [11] B. Baller, “Liquid argon TPC signal formation, signal processing and reconstruction techniques,” *JINST* **12** no. 07, (2017) P07010 FERMILAB-PUB-15-458-ND, arXiv:1703.04024 [physics.ins-det].
- [12] MicroBooNE Collaboration, R. Acciarri *et al.*, “The Pandora multi-algorithm approach to automated pattern recognition of cosmic-ray muon and neutrino events in the MicroBooNE detector,” *Eur. Phys. J.* **C78** no. 1, (2018) 82 FERMILAB-PUB-17-306-ND, arXiv:1708.03135 [hep-ex].
- [13] X. Qian, C. Zhang, B. Viren, and M. Diwan, “Three-dimensional Imaging for Large LArTPCs,” arXiv:1803.04850 [physics.ins-det].
- [14] MicroBooNE Collaboration, R. Acciarri *et al.*, “Convolutional Neural Networks Applied to Neutrino Events in a Liquid Argon Time Projection Chamber,” *JINST* **12** no. 03, (2017) P03011 FERMILAB-PUB-16-538-ND, arXiv:1611.05531 [physics.ins-det].
- [15] MicroBooNE Collaboration, “First Muon-Neutrino Charged-Current Inclusive Differential Cross Section Measurement for MicroBooNE Run 1 Data,” MICROBOONE-NOTE-1045-PUB.
- [16] V. L. Highland, “Some Practical Remarks on Multiple Scattering,” *Nucl. Instrum. Meth.* **129** (1975) 497 Print-75-0993 (TEMPLE).
- [17] Particle Data Group Collaboration, C. Patrignani *et al.*, “Review of Particle Physics,” *Chin. Phys.* **C40** no. 10, (2016) 100001.
- [18] R. E. Kalman, “A new approach to linear filtering and prediction problems,” *ASME Journal of Basic Engineering* (1960) .
- [19] R. Fruhwirth, “Application of Kalman filtering to track and vertex fitting,” *Nucl. Instrum. Meth.* **A262** (1987) 444–450 HEPHY-PUB-87-503.
- [20] G. Bradski, “The OpenCV Library,” *Dr. Dobb’s Journal of Software Tools* (2000) .

- [21] E. L. Snider and G. Petrillo, “LArSoft: Toolkit for Simulation, Reconstruction and Analysis of Liquid Argon TPC Neutrino Detectors,” *J. Phys. Conf. Ser.* **898** no. 4, (2017) 042057 FERMILAB-CONF-17-052-CD.
- [22] MicroBooNE Collaboration, “MicroBooNE Detector Stability,” MICROBOONE-NOTE-1013-PUB.
- [23] C. Andreopoulos *et al.*, “The GENIE Neutrino Monte Carlo Generator,” *Nucl. Instrum. Meth.* **A614** (2010) 87–104 FERMILAB-PUB-09-418-CD, [arXiv:0905.2517 \[hep-ph\]](#).
- [24] D. Heck, G. Schatz, T. Thouw, J. Knapp, and J. N. Capdevielle, “CORSIKA: A Monte Carlo code to simulate extensive air showers,” FZKA-6019.
- [25] GEANT4 Collaboration, S. Agostinelli *et al.*, “GEANT4: A Simulation toolkit,” *Nucl. Instrum. Meth.* **A506** (2003) 250–303 SLAC-PUB-9350, FERMILAB-PUB-03-339.
- [26] MicroBooNE Collaboration, “First Measurement of Muon Neutrino Charged Current Neutral Pion Production on Argon with the MicroBooNE LArTPC,” MICROBOONE-NOTE-1032-PUB.
- [27] MicroBooNE Collaboration, C. Adams *et al.*, “Comparison of  $\nu_\mu$ -Ar multiplicity distributions observed by MicroBooNE to GENIE model predictions,” [arXiv:1805.06887 \[hep-ex\]](#).
- [28] MicroBooNE Collaboration, B. Fleming *et al.*, “The MicroBooNE Technical Design Report,” FERMILAB-DESIGN-2012-04.